JOURNAL OF PROPULSION AND POWER
Vol. 14, No. 2, March–April 1998

Three-Dimensional Turbine Rotor Forcing Functions and Linear Theory Analysis

David A. Johnston* and Sanford Fleeter†
Purdue University, West Lafayette, Indiana 47907

Many turbomachine flowfields are inherently three dimensional. Often, however, the data and methods used to analyze the unsteady aerodynamic forcing functions generated by these blade rows are two dimensional. This paper is directed at developing a three-dimensional compressible flow forcing-function modeling technique to split forcing-function data into vortical and potential components. This is accomplished by extending current state-of-the-art two-dimensional methods to three dimensions in cylindrical coordinates. Three-dimensional unsteady forcing-function data, both unsteady pressure and velocity, generated by the first rotor of a low-speed, two-stage research turbine are used in the model development. Both the three-dimensional model developed herein and a two-dimensional model are then applied to the turbine rotor data. For the potential perturbation velocity, the three-dimensional method agrees well with the two-dimensional strip theory method in terms of both velocities and axial decay factors. For the vortical perturbation velocity, the correlations were inconsistent with the two-dimensional theory in that the vortical proportionality constant was not constant and the phasing of the velocity components was not zero.

Nomenclature

A, D = potential and vortical perturbation proportionality constants
c = speed of sound
J_ν, Y_ν = Bessel functions of the first and second kinds of order ν
k = wave number
M = Mach number of relative mean flow
P = mean pressure
p = perturbation pressure
S_R = rotor blade spacing
s, τ = streamwise and transverse coordinates
U, V, W = axial, tangential, and radial mean velocity components of $\boldsymbol{Q}$
u, v, w = axial, tangential, and radial perturbation velocity components of $\boldsymbol{v}$
$\boldsymbol{\beta}$ = relative exit flow angle
$\boldsymbol{\lambda}$ = eigenvalue for eigenfunction in r
ϕ = potential function of perturbation quantities
χ = complex axial decay factor
ς = phase angle

Subscripts

H, T = hub and tip
p, v = potential and vortical
θ, x = tangential and axial
0 = uniform freestream

Superscripts

$+$ = magnitude or phase angle
$*$ = nondimensionalized by Q or $\rho_0 Q^2$

Received April 15, 1997; revision received Aug. 27, 1997; accepted for publication Sept. 18, 1997.

*Graduate Research Assistant, School of Mechanical Engineering. Student Member AIAA.

†McAllister Distinguished Professor, School of Mechanical Engineering. Associate Fellow AIAA.

Introduction

FLOWFIELDS in multistage turbomachinery are unsteady because of flow phenomena such as inlet distortion, viscous wakes, secondary flows, turbulence, shock waves, and potential fields producing irregular flow patterns. The relative motion between adjacent blade rows causes the flow spatial nonuniformity of one row to produce temporal flow fluctuations (aerodynamic forcing functions) to an adjacent row. These increase blade heat transfer and can produce blade vibrations that adversely affect blade durability and fatigue life.

Many unsteady aerodynamic models to predict blade response rely on linearization of the equations describing the two-dimensional, inviscid flowfield. The unsteady flow is assumed to be composed of a small vortical or potential perturbation to a steady flow. Depending on the model, the steady flow is treated as either a uniform potential or an Euler flowfield. Additionally, nonlinear, two-dimensional unsteady Euler and three-dimensional unsteady Navier–Stokes analyses exist but require considerably more computational time than the more prevalent linearized, two-dimensional models.

Henderson and Fleeter[1] experimentally investigated the two-dimensional vortical gust modeling assumption of the linearized, two-dimensional model. Forcing functions generated by perforated plates satisfied vortical gust constraints, but those generated by loaded airfoils did not. As a result of the large unsteady static pressure perturbations present in the airfoil gusts, they suggested that better data–theory correlation would be achieved by additionally modeling and incorporating the potential component of the gust into their forcing-function model.

Manwaring and Wisler[2] incorporated the potential component of the gust in the forcing-function model by using the two-dimensional analysis method and applied the resulting analysis to low-speed research turbine and compressor data. The measured gusts are split into vortical and potential components using only the measured unsteady velocity data.

Feiereisen et al.[3] determined, through a weighted least-squares study of two-dimensional unsteady data from a rotating annular cascade, that proper splitting of forcing function data requires the measurement of the unsteady pressure in addition to the unsteady velocity. This was determined by parametrically weighting the pressure data from zero to full

weighting and comparing the results to theory. This method has also been applied to low-speed turbine data.[4] As a result, a non-least-squares two-dimensional method was developed that fully uses both pressure and velocity measurements and has been applied to compressor data.[5,6]

Many turbomachine flowfields, particularly turbine flows, are inherently three dimensional. However, the previously noted data and methods used to analyze the unsteady aerodynamic forcing functions generated by these blade rows are two dimensional. Thus, this paper is directed at developing a three-dimensional compressible flow forcing-function modeling technique to split forcing-function data into vortical and potential components and then assessing three-dimensional turbine rotor forcing functions. This is accomplished by extending the two-dimensional methods developed by Feiereisen et al.[3] to three dimensions and considering the steady flow to be compressible and uniform. Three-dimensional unsteady forcing-function data, both unsteady pressure and velocity, generated by the first rotor of a low-speed, two-stage research turbine are used to aid in the model development. Both the three-dimensional model developed herein and a two-dimensional model are then used to split the measured forcing function gusts into potential and vortical components, with the two- and three-dimensional results correlated.

Research Turbine

The Purdue Low-Speed Research Turbine is a 2500-rpm two-stage axial-flow turbine with constant hub and tip diameter (Fig. 1) and 50% reaction NACA A_3K_7 series airfoils. Air at ambient pressure and temperature is drawn into the turbine inlet by a centrifugal blower powered by a 100-hp (75-kW) electric motor. Airflow rates of 3000–5400 scfm (1.4–2.6 m^3/s) are measured by a 20-in.-diam (0.51-m Ø) venturi flow meter and regulated by a variable inlet vane damper, enabling the turbine flow coefficient to be varied from 0.3 to 0.5. Turbine loading is controlled by a water brake dynamometer that dissipates 40 hp (30 kW) at the highest turbine loading, enabling the turbine-stage loading coefficient to be varied from 0.4 to 1.8. Additional turbine design details are as follows: flow rate 5.6 lbm/s (2.5 kg/s), axial velocity 91 ft/s (28 m/s), rotational speed 2500 rpm, number of stages 2, power extraction 30 hp (22 kW), reaction 50%, tip diameter 19.18 in. (0.49 m), hub/tip ratio 0.740, flow coefficient 0.47, and stage loading coefficient 1.52. Turbine cascade geometry is shown in Table 1.

Instrumentation

Spanwise unsteady static pressure measurements are made using a 0.095-in.-diam (2.4-mm) probe constructed from a Kulite XCS-062 ultraminiature transducer mounted on a Mitutoyu digital scale with 0.001-in. (25-μm) resolution. The pressure probe is calibrated for pitch and yaw angle sensitivity. Unsteady, three-dimensional velocity measurements are made with a TSI 1213-20 hot-film slant probe. The cylindrical sensor of the slant probe is 0.002-in. diam (51-μm), 0.040-in. (1.0 mm) long, and slanted at 45 deg. The slant sensor is moved along the span and rotated about the probe axis with an L. C. Smith Co. actuator having 0.02-in. (0.51-mm) linear resolution and 0.2-deg angular resolution. Voltage signals from the pressure and slant probes are taken using a National Instruments A-2000 A/D data acquisition board.

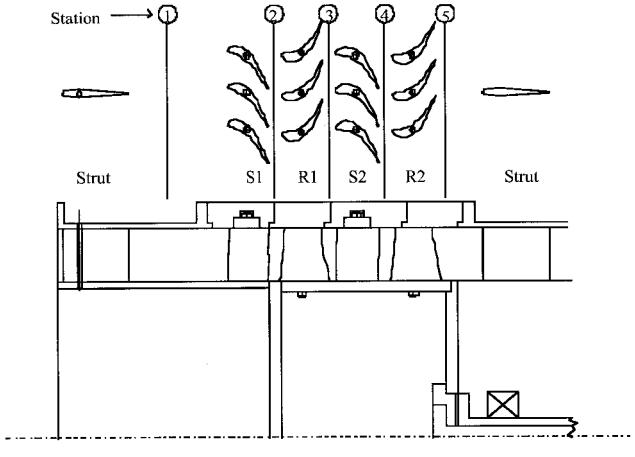

Fig. 1 Purdue Low-Speed Research Turbine facility.

Table 1 Turbine cascade geometry

	Stator 1	Rotor 1	Stator 2	Rotor 2
No. of blades	32	29	32	31
Chord, in. (mm)	2.5 (64)	2.5 (64)	2.5 (64)	2.5 (64)
Aspect ratio	1.0	1.0	1.0	1.0
Solidity	1.53	1.38	1.53	1.48

Data Acquisition and Analysis

Probes are located a quarter-chord axially downstream of the first-stage rotor trailing edge at the inlet plane of the second-stage stator. Data are acquired from 10 to 90% span in 10%-span increments. The hot-film slant and pressure probes are located 22.5 deg apart circumferentially, with each probe situated halfway between adjacent stators of stage two.

Data are acquired at the turbine design flow coefficient of 0.47. The data sampling rate is approximately 24 kHz, resulting in 20 data points per rotor blade, with gusts from 10 blades acquired per rotor revolution to comprise one frame of data. The sampling frequency is adjusted so that exactly 10 rotor blade gusts are acquired per frame to ensure against leakage in the Fourier transform analysis. Each frame of data is synchronized or phase locked in that each is triggered by a one-per-revolution optical trigger mounted on the turbine shaft. This allows the frames to be ensemble-averaged to eliminate nonperiodic random fluctuations in the data signals. For each spanwise location, 200 frames are acquired for ensemble-averaging. Because the pressure probe is at a different circumferential location than the hot-film slant probe, after Fourier transformation of the pressure and velocity signals the pressure signal is phase shifted to correspond to the location of the velocity signal. The estimated measurement uncertainties are ±2% for static pressure, ±6% for velocity magnitude, ±2 deg for velocity direction, and ±1/2% for spanwise location.

Linear Theory

For an unsteady, isentropic, compressible flow composed of a uniform mean flow and a small-perturbation unsteady flow, the linearized continuity and momentum equations describing the perturbation velocity and pressure are

$$\frac{1}{c_0^2}\frac{\mathrm{D}_0 p}{\mathrm{D}t} + \rho_0 \nabla \cdot \boldsymbol{v} = 0 \tag{1}$$

$$\rho_0 \frac{\mathrm{D}_0 \boldsymbol{v}}{\mathrm{D}t} + \nabla p = 0 \tag{2}$$

where the velocity $\boldsymbol{v}$ and pressure p are small compared to the mean velocity and pressure, ρ_0 and c_0 are the constant free-stream density and speed of sound, respectively, and the material derivative is $\mathrm{D}_0/\mathrm{D}t \equiv \partial/\partial t + \boldsymbol{Q}\cdot\nabla$, where $\boldsymbol{Q}$ is the mean velocity vector.

Velocity Field Decomposition

The perturbation velocity field is decomposed into vortical (rotational) and potential (irrotational) components[7]

$$\boldsymbol{v} = \boldsymbol{v}_v + \boldsymbol{v}_p \tag{3}$$

where the rotational velocity is termed vortical, and the irrotational velocity is termed potential.

The vortical velocity is constrained to be solenoidal and convective

$$\nabla \cdot \boldsymbol{v}_v = 0 \tag{4}$$

$$\frac{\mathrm{D}_0 \boldsymbol{v}_v}{\mathrm{D}t} = \boldsymbol{0} \tag{5}$$

and the potential velocity satisfies

$$\boldsymbol{v}_p = \nabla \boldsymbol{\phi} \tag{6}$$

$$\nabla \times \boldsymbol{v}_p = \boldsymbol{0} \tag{7}$$

Substituting these relations into Eq. (2) yields the unsteady, linearized Bernoulli equation, and from Eq. (1), the convective wave equation:

$$p = -\rho_0 \frac{\mathrm{D}_0 \boldsymbol{\phi}}{\mathrm{D}t} \tag{8}$$

$$\frac{1}{c_0^2} \frac{\mathrm{D}_0}{\mathrm{D}t} \frac{\mathrm{D}_0}{\mathrm{D}t} \phi - \nabla^2 \phi = 0 \tag{9}$$

Vortical Gust

The solution to Eq. (5) is the real part of

$$\boldsymbol{v}_v = \boldsymbol{v}_v^+ \exp[-i\boldsymbol{k} \cdot (\boldsymbol{x} - \boldsymbol{Q}t) - i\varsigma^+] \tag{10}$$

where the gust propagation vector for two-dimensional flow in terms of x and θ coordinates is $\boldsymbol{k} \equiv k_x \hat{e}_x + k_\theta \hat{e}_\theta$, and the constant, real gust magnitude vector is $\boldsymbol{v}_v^+ \equiv u_v^+ \hat{e}_x + v_v^+ \hat{e}_\theta$.

With respect to the rotor frame of reference wherein the flow is steady, substituting Eq. (10) into Eq. (4) yields

$$u_v^+ k_x + v_v^+ k_\theta = 0 \tag{11}$$

From geometric consideration of the rotor exit flowfield in the relative reference frame (Fig. 2), the gust propagation vector is perpendicular to the mean relative velocity vector, expressed as $\boldsymbol{k} \cdot \boldsymbol{Q} = 0$, or in expanded form

$$Uk_x + Vk_\theta = 0 \tag{12}$$

where the wave number vector components are $k_\theta = 2\pi/S_R$, and $k_x = -k_\theta \tan \bar{\boldsymbol{\beta}}$, $\bar{\beta}$ is the mean relative exit flow angle.

Equations (11) and (12) imply proportionality between the vortical gust vector and the mean relative velocity vector, with the proportionality constant denoted as D. Equation (10) expressed in the rotor relative reference frame is thus

$$\boldsymbol{v}_v = D\boldsymbol{Q} \exp(-i\boldsymbol{k} \cdot \boldsymbol{x}) \tag{13}$$

This implies that the vortical gust maintains constant amplitude and phase as it convects, known as the frozen gust assumption, meaning that the gust is unaffected by the local steady potential field.

Equation (13) represents a planar wave. Hence, Eq. (13) is valid only when the three-dimensional region may be well described by a Cartesian coordinate system, i.e., the curvature of the annulus must be small compared to the blade pitch spacing and span. Thus, for flows that are better modeled in the three-dimensional cylindrical r, θ, x coordinate system

$$\boldsymbol{v}_v \not\propto \boldsymbol{Q} \tag{14}$$

$$\boldsymbol{v}_v \neq D\boldsymbol{Q} \exp(-i\boldsymbol{k} \cdot \boldsymbol{x}) \tag{15}$$

Potential Gust

In the steady, two-dimensional rotor frame of reference, Eq. (9) simplifies to

$$(1 - M^2) \frac{\partial^2 \phi}{\partial s^2} + \frac{\partial^2 \phi}{\partial \tau^2} = 0 \tag{16}$$

Applying periodicity boundary conditions in the tangential direction and boundedness in the positive axial direction, solutions are obtained in the axial–coordinate system

$$\phi = \sum_{n=-\infty}^{\infty} A_n \exp[k_\theta(|n|\chi x - in\theta)] \tag{17}$$

where A is a complex constant and χ is given by

$$\chi \equiv \frac{iM^2 \cos \bar{\beta} \sin \bar{\beta} - \sqrt{1 - M^2}}{1 - M^2 \cos^2 \bar{\beta}} \tag{18}$$

Similarly, the following three-dimensional solution to Eq. (16) in cylindrical coordinates is obtained by applying periodicity boundary conditions in the tangential direction, flow tangency at the hub and tip walls, and boundedness in the positive axial direction:

$$\phi = \sum_{m=1}^{\infty} \sum_{n=-\infty}^{\infty} C_{m,n} R(\boldsymbol{\lambda}_{m,n}, r) \exp(-\lambda_{m,n} x - ink_\theta \theta) \tag{19}$$

$C_{m,n}$ are complex coefficients, and eigenfunctions R are given by

$$R(\lambda_{m,n}, r) \equiv \frac{J_\nu(\lambda_{m,n} r)}{\lambda_{m,n} J'_\nu(\lambda_{m,n} r_T)} - \frac{Y_\nu(\lambda_{m,n} r)}{\lambda_{m,n} Y'_\nu(\lambda_{m,n} r_T)} \tag{20}$$

the primes denote differentiation with respect to r, $\nu = |n| k_\theta$, and the eigenvalues are the positive roots of

$$\frac{J'_\nu(\lambda_{m,n} r_H)}{J'_\nu(\lambda_{m,n} r_T)} - \frac{Y'_\nu(\lambda_{m,n} r_H)}{Y'_\nu(\lambda_{m,n} r_T)} = 0 \tag{21}$$

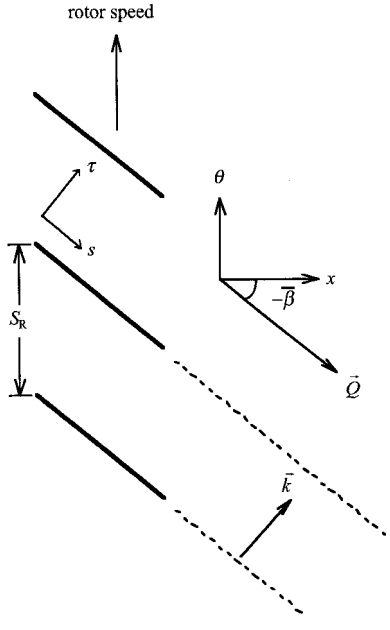

Fig. 2 Rotor relative exit flowfield.

r_H and r_T are the constant hub and tip radii, respectively. Therefore this solution is restricted to rotor geometries of constant hub and case radii.

By superposition and without loss of generality the perturbation velocity and pressure series solutions may be represented by a single term of the series in n. Applying Eq. (19) to Eqs. (6) and (8) yields the following relations for the perturbation quantities corresponding to the first harmonic of rotor blade pass frequency ($n = 1$).

For the two-dimensional case the perturbation quantities resulting from the potential at some location $x = 0$ are

$$u_p = -k_\theta A \tag{22}$$

$$v_p = -ik_\theta A \tag{23}$$

$$p = \rho_0 k_\theta A(U + iV) \tag{24}$$

For a three-dimensional flow at some point $x = 0$ the perturbation quantities resulting from the potential are

$$u_p = \sum_{m=1}^{\infty} -\lambda_m C_m R(\lambda_m, r) \tag{25}$$

$$v_p = \sum_{m=1}^{\infty} -i\frac{k_\theta}{r} C_m R(\lambda_m, r) \tag{26}$$

$$w_p = \sum_{m=1}^{\infty} C_m R'(\lambda_m, r) \tag{27}$$

$$p = \sum_{m=1}^{\infty} \rho_0 C_m \left[\left(U\lambda_m + Vi\frac{k_\theta}{r}\right) R(\lambda_m, r) - WR'(\lambda_m, r)\right] \tag{28}$$

Analytical Procedure

For a two-dimensional flow with spanwise pressure and velocity data acquired and Fourier transformed to extract the first harmonic of rotor blade pass frequency, A is calculated from Eq. (24). The potential velocity v_p is then calculated using Eqs. (22) and (23). The vortical velocity v_v is found from Eq. (3), i.e., the potential velocity is subtracted from the measured velocity yielding the vortical velocity. The proportionality constant D is then determined from

$$D = \frac{u_v \cos\bar{\beta} + v_v \sin\bar{\beta}}{\sqrt{U^2 + V^2}} \tag{29}$$

which is derived from the definition of vorticity and Eq. (13).

For the three-dimensional case, starting with Eq. (28), the only unknown is C_m. The eigenfunctions R are orthogonal on the interval $r \in [r_T, r_H]$, but the first derivatives of the eigenfunctions in Eq. (28) are not, thereby precluding the solution for C_m by integration over the interval. However, $R'(\lambda_m, r)$ and $(k_\theta/r)R(\lambda_m, r)$ and $\lambda_m R(\lambda_m, r)$ are approximately equal in amplitude, whereas $U/Q \approx 0.50$, $V/Q \approx 0.86$, and $W/Q \approx 0.06$, where

$$Q = \sqrt{U^2 + V^2 + W^2}$$

Therefore, from an order-of-magnitude analysis of the data, the derivative term of R is neglected so that Eq. (28) may now be solved for C_m per orthogonality of R.

With C_m determined by numerical integration, u_p, v_p, and w_p are found from Eqs. (25–27). (Six terms are used in the series expansion in m.) The vortical velocities are then found using Eq. (3), per the two-dimensional case.

Results

Temporal mean values of the radial W^*, tangential V^*, and axial U^* velocity components, and pressure P^* at each spanwise location are shown in Fig. 3. The velocity values are nondimensionalized by Q (the magnitude of the mean velocity vector), and the pressure by $\rho_0 Q^2$. The mean flow is fairly uniform, with spatial variations of less than 10% in the tangential velocity across the span. The mean radial velocity is small compared to the axial or tangential velocities. Corresponding perturbation values of first Fourier harmonic magnitude are shown in Fig. 4. The radial perturbation dominates the unsteady flow from the hub to midspan, otherwise, velocities are of similar magnitude.

The magnitudes of the potential radial, tangential, and axial velocity perturbation components are shown in Figs. 5, 6, and 7, respectively. From 10 to 40% span, the radial perturbation velocity is small compared to the tangential and axial perturbation velocities that are nearly equal. Figures 6 and 7 show a comparison of the potential perturbation velocities calculated from the two- and three-dimensional formulations. The two- and three-dimensional potential perturbation velocities, both tangential and axial, compare well in both magnitude and phase (phase not shown). The three-dimensional method predicts a radial perturbation, even when the mean radial flow is negligible, of which the two-dimensional method is incapable.

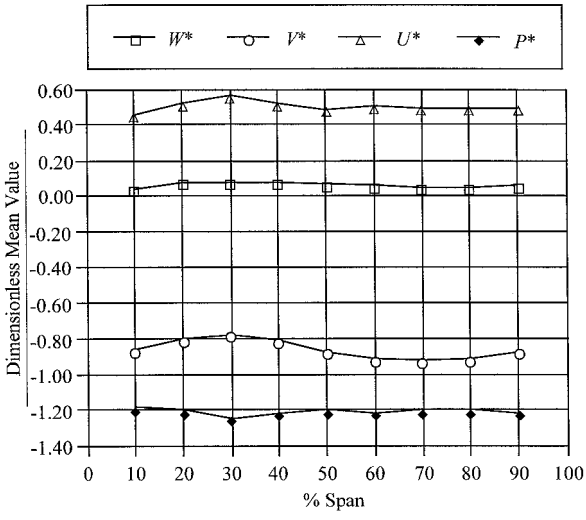

Fig. 3 Spanwise variation of mean velocity and pressure.

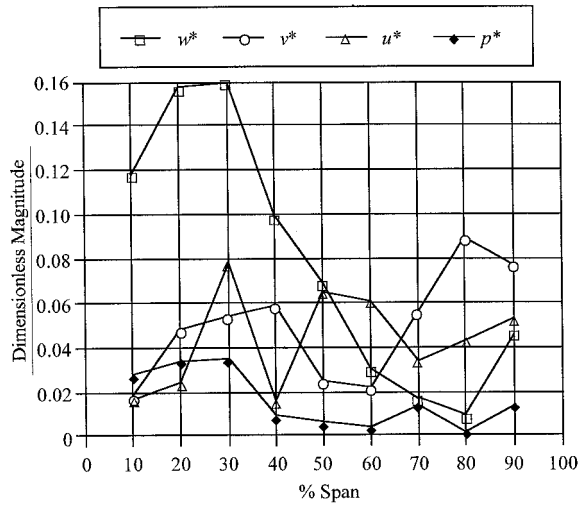

Fig. 4 Spanwise variation of first harmonic perturbation velocities and pressure.

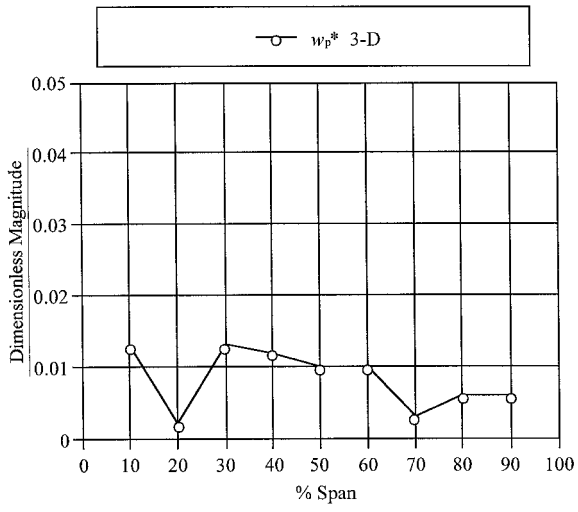

Fig. 5 Potential perturbation radial velocity, three-dimensional analysis.

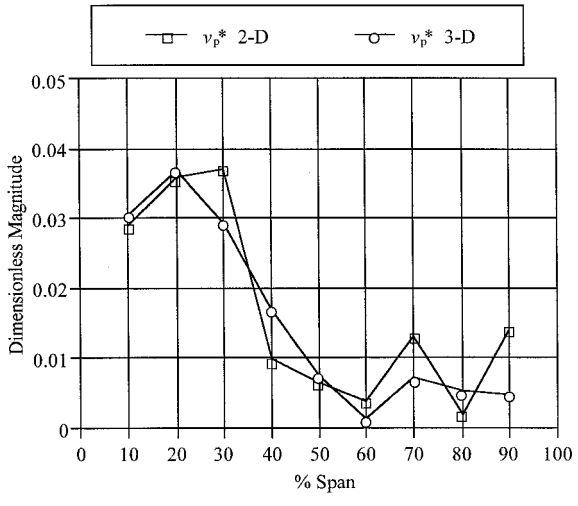

Fig. 6 Potential perturbation tangential velocity, two- and three-dimensional analyses.

Another comparison between the two- and three-dimensional methods for the potential perturbations is to compare the theoretical axial decay. For the two-dimensional method, the axial decay factor from Eq. (18) is $k_x = -nk_\theta$, and with the three-dimensional method the axial decay factor is $k_x = -\lambda_{m,n}$ specified in Eq. (19). The dominant axial decay factor occurs when $n = 1$ and $m = 0$; for this case, the two-dimensional axial decay factor is -3.45 in.$^{-1}$ (-0.136 mm^{-1}), whereas it is -3.87 in.$^{-1}$ (-0.152 mm^{-1}) for the three-dimensional method, a 12% difference.

The two-dimensional linear theory requires the axial and tangential potential perturbation velocity components to be 90 deg out of phase, and the phase difference between the axial and tangential vortical velocity components to be either 0 or 180 deg. Figure 8a shows the phase difference, tangential minus axial, between perturbation velocity components obtained with the two-dimensional method. The potential phasing is indeed 90 deg, and the vortical phasing is near 180 deg, although not consistently for all spanwise locations.

In contrast, as a result of the series summation in r, the three-dimensional theory does not restrict the phasing of the axial and tangential potential perturbation velocity components to be 90 deg. Figure 8b shows the phase differences obtained with the three-dimensional method. The potential perturbation velocity components are not consistently 90-deg out of phase as in the two-dimensional case, but the vortical phasing is nearly equal to the measured perturbation velocity phasing for the 50–90% span range, analogous to the two-dimensional results.

If the phase difference of the potential perturbation velocity components is 90 deg, and the vortical velocity components are 0- or 180-deg out of phase as dictated by two-dimensional linear theory, then the velocity vector plot of the first harmonic gust perturbation would appear as in Fig. 9, which shows in the $x-\theta$ plane the measured velocity vector (u, v) and its constituents (u_p, v_p) and (u_v, v_v), with the solid curve representing p. Per linear theory,[1] the vortical axial and tangential perturbation velocity vector phasing is 0 or 180 deg, producing par-

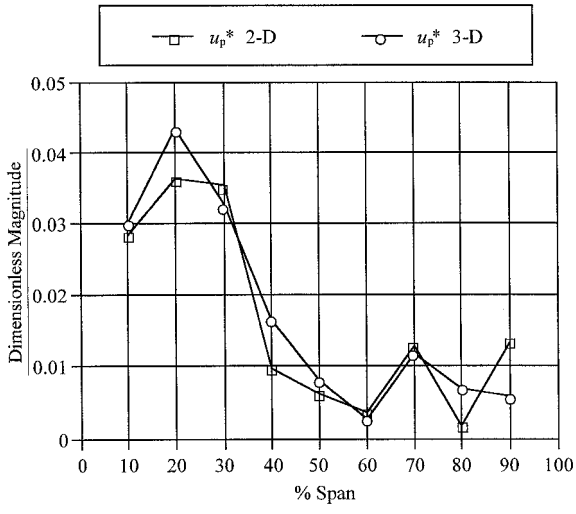

Fig. 7 Potential perturbation axial velocity, two- and three-dimensional analyses.

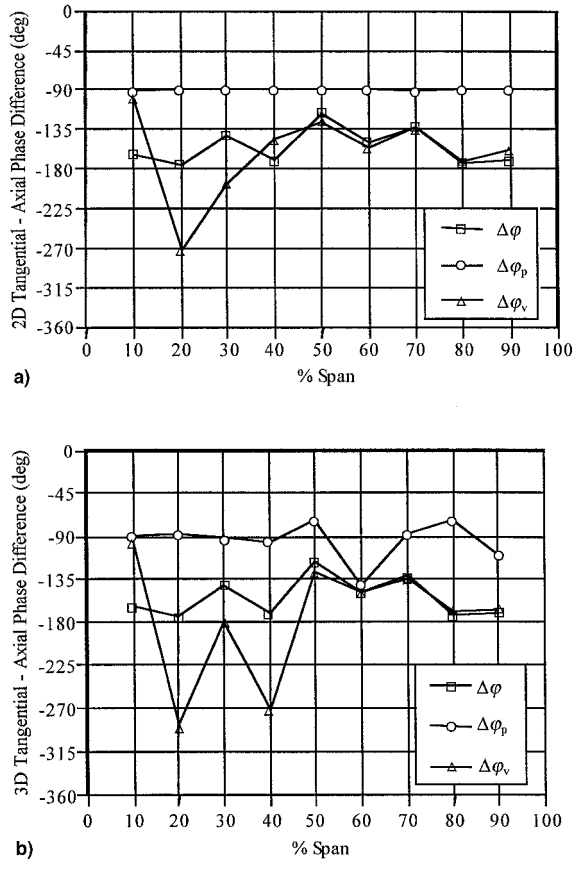

Fig. 8 Phase differences: a) two- and b) three-dimensional analyses.

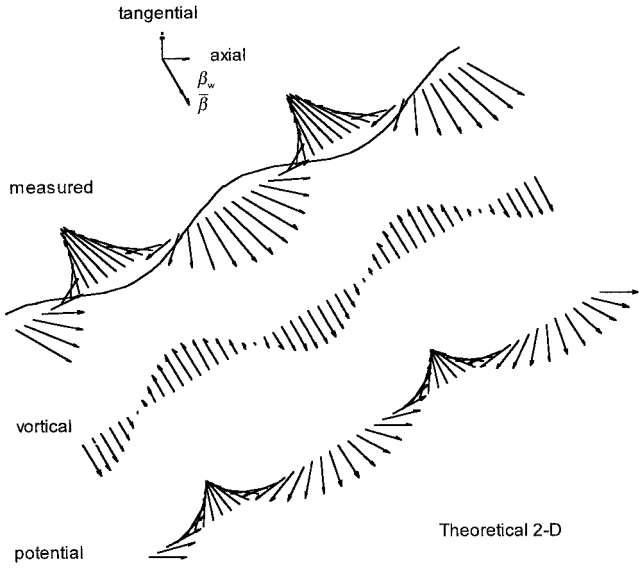

Fig. 9 Linear theory two-dimensional gusts.

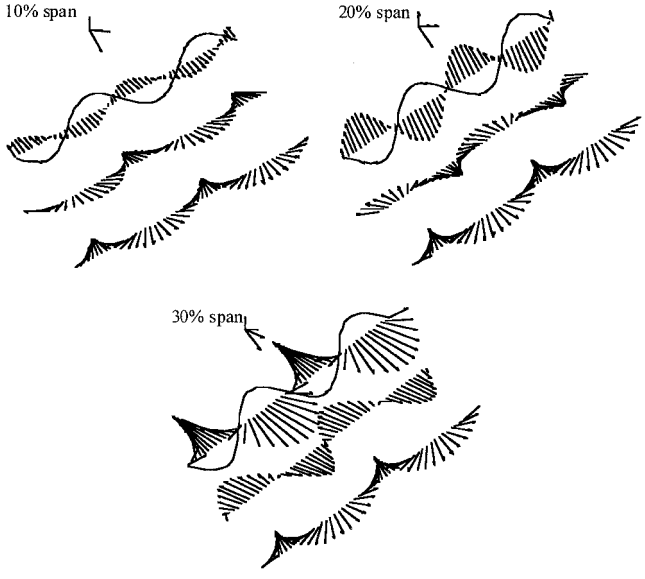

Fig. 10 Hub region gusts.

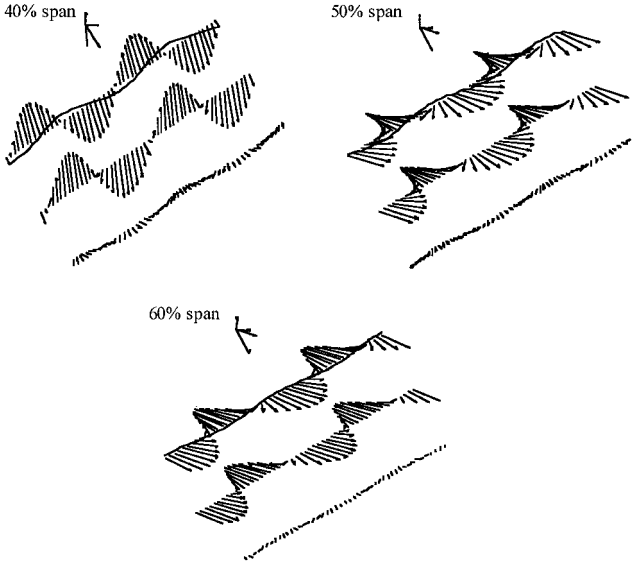

Fig. 11 Midspan region gusts.

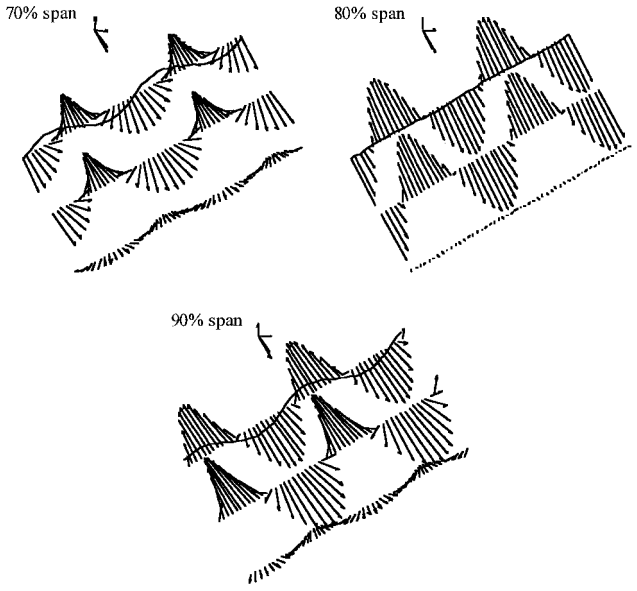

Fig. 12 Tip region gusts.

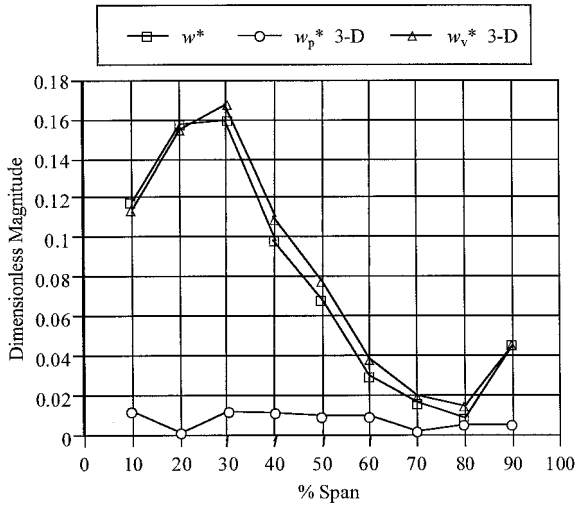

Fig. 13 Turbine rotor perturbation radial velocity component.

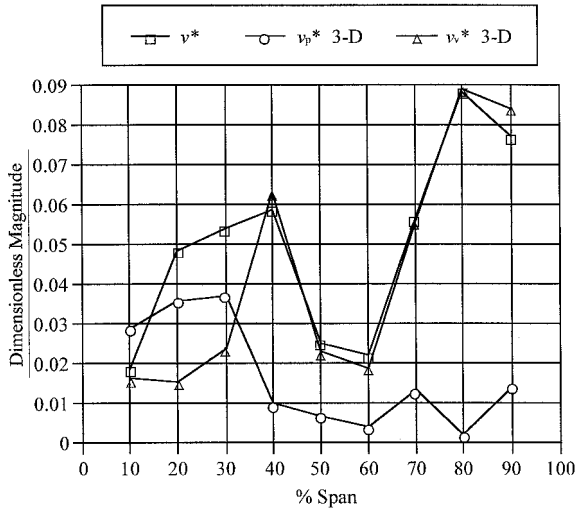

Fig. 14 Turbine rotor perturbation tangential velocity component.

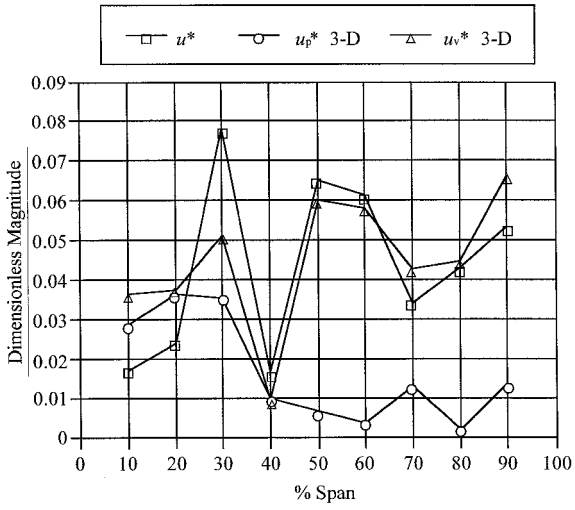

Fig. 15 Turbine rotor perturbation axial velocity component.

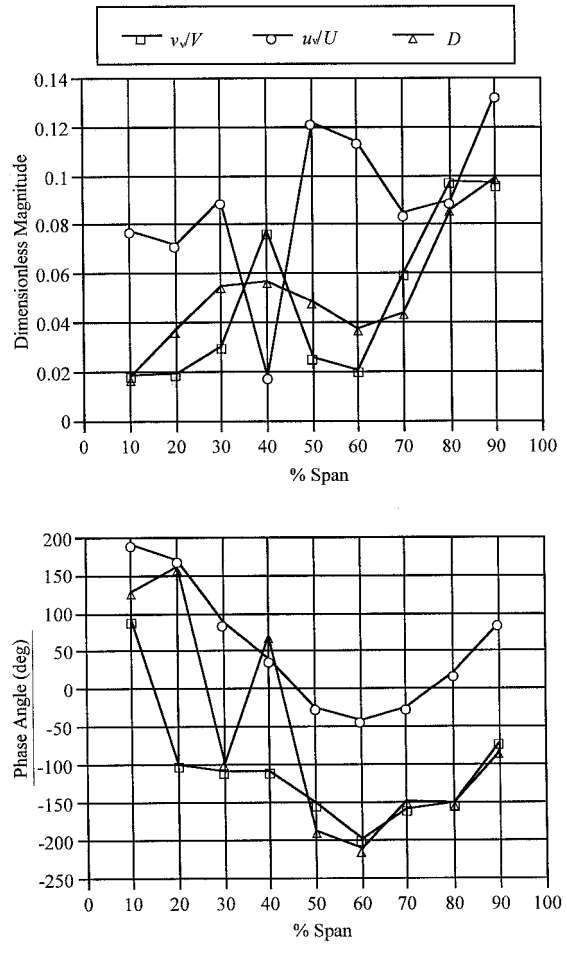

Fig. 16 Comparison of two-dimensional theory proportionality constant D to vortical velocity ratios.

allel vectors, and the relative flow angle, i.e., the flow angle when the vortical velocity magnitude is a maximum, termed the gust magnitude direction β_w, is equal to the mean relative flow angle, i.e., $\bar{\beta} = \beta_w$. In Fig. 9, $\bar{\beta}$ is measured from axial to the longer of the two nonperpendicular arrows, with β_w measured from axial to the shorter of the two nonperpendicular arrows.

Figures 10–12 show the first harmonic gust vector data for 10–90% span. In general, $\bar{\beta} \neq \beta_w$, but at 20, 70, 80, and 90% span, the two angles are nearly equal. The phase difference of the vortical velocity components is not 0 or 180 deg, but at 40 and 80% span, the vortical velocity vectors are nearly parallel. Gust plots (not shown) obtained with the three-dimensional method are indistinguishable from the results of Figs. 10–12, which were generated using the two-dimensional potential velocity. This is a result of the similarity between the two- and three-dimensional potential velocity cases shown in Figs. 6 and 7.

Figures 13–15 show the first harmonic magnitudes of the radial, tangential, and axial potential and vortical velocity perturbation data, respectively. From 40 to 90% span, the vortical perturbation velocity component is dominant. However, for the radial perturbation velocity component, the vortical velocity is dominant over the entire span.

Figure 16 compares the calculated values of D [Eq. (29)] to the ratio of the vortical velocity component to the mean velocity component. From two-dimensional linear theory, $D = u_v/U = v_v/V$ and D = constant. From the data, D is of the same order of magnitude as the vortical velocity ratios, but is generally not equal to them or constant. Further, the vortical velocity ratios are not equal. However, the phase angle of D is nearly equal to the phase angle of one of the two velocity ratios.

Summary and Conclusions

To address the three-dimensional flowfields inherent in turbomachines, a three-dimensional compressible forcing-function modeling technique to split forcing-function data into vortical and potential components was developed. This was accomplished by extending state-of-the-art two-dimensional methods, with the steady flow considered to be uniform and compressible. Three-dimensional unsteady forcing-function data, both unsteady pressure and velocity, produced by the first rotor of a low-speed, two-stage research turbine were used in the model development. Both the three-dimensional model developed herein and a two-dimensional model were then used to split the measured forcing-function gusts into potential and vortical components, with the two- and three-dimensional results correlated.

For the potential perturbation velocity the three-dimensional method agrees well with the two-dimensional method applied in strip theory fashion. Also, the two- and three-dimensional axial decay factors differ by only 12%. The three-dimensional method predicts radial perturbations, even if the mean radial flow is small or zero, of which the two-dimensional method is incapable.

For the vortical perturbation velocity the proportionality constant D is not constant, but instead varies with span. Also, the phasing of the vortical velocities is generally not in congruence with the two-dimensional theoretical phasing. These experimental results are consistent with the three-dimensional model developed herein, which showed that simple proportionality between the perturbation and mean velocities does not exist for flow regions that are best described by the three-dimensional cylindrical coordinate system because of curvature.

Finally, regarding the measured velocity field, the fraction of the measured perturbation velocity that is potential or vortical varies with span. The perturbation velocity field is dominated by the vortical velocity from 40 to 90% span. Also of note is that near the hub the radial perturbation velocity dominates from 10 to 50% span.

Acknowledgment

This research was sponsored, in part, by the Army Research Office (ARO). This support is most gratefully acknowledged.

References

[1]Henderson, G. H., and Fleeter, S., "Forcing Function Effects on Unsteady Aerodynamic Gust Response, Part 1: Forcing Functions," *Journal of Turbomachinery*, Vol. 115, No. 4, 1992, pp. 741–750.

[2]Manwaring, S. R., and Wisler, D. C., "Unsteady Aerodynamics

and Gust Response in Compressors and Turbines," American Society of Mechanical Engineers, Paper 92-GT-422, June 1992.

[3]Feiereisen, J. M., Montgomery, M. D., and Fleeter, S., "Unsteady Aerodynamic Forcing Functions: A Comparison Between Linear Theory and Experiment," American Society of Mechanical Engineers, Paper 93-GT-141, May 1993.

[4]Weaver, M. M., and Fleeter, S., "Turbine Rotor Generated Forcing Functions for Flow Induced Vibrations," American Society of Mechanical Engineers, Paper 94-GT-328, June 1994.

[5]Feiereisen, J., and Fleeter, S., "Low Solidity Vane Unsteady Aerodynamic Response to Combined Vortical-Potential Forcing Functions," AIAA Paper 94-2974, June 1994.

[6]Johnston, R. T., Feiereisen, J. M., and Fleeter, S., "High Speed Axial Fan Stage Wakes for Application to Flow Induced Vibration Prediction," AIAA Paper 94-2975, June 1994.

[7]Goldstein, M. E., "Unsteady Vortical and Entropic Distortions of Potential Flows Around Arbitrary Obstacles," *Journal of Fluid Mechanics*, Vol. 89, Pt. 3, 1978, pp. 433–468.